

Supplementary Materials for Wind-Driver: A Framework for High-Maneuverability Planning and High-Precision Control for Quadrotor Autopilots

Yuyang Wang, Jindou Jia, Zeshuai Chen, Kexin Guo, Xiang Yu*, and Lei Guo

I. GUIDELINES TO ADJUST RELATED PARAMETERS

It can be seen that there are respectable parameters that need to adjust in both the simulation and experiment. For different quadrotors, the values of these parameters may vary, but the tuning methods remain the same. The proposed framework can be applied to different quadrotor platforms. Here several guidelines are provided for quickly tuning key parameters.

A. Parameters related to the propeller

The parameters related to the propeller k_m, k_w, k_z, k_h should be obtained through fitting measurements, as detailed in [1], [2]. These parameters are only influenced by the type of the quadrotor and its propeller. They are independent of external environmental factors (such as wind conditions). If the quadrotor hardware is changed, these parameters need to be re-measured and fitted.

B. The weights in the back-end trajectory optimization

In Section IV.B, the cost function is formulated by minimizing the dynamic feasibility F_f , energy conservation F_e , and collision safety F_c of the trajectory. The parameters k_f, k_e, k_c represent the weights of each component in the optimization problem. In order to ensure that the final trajectory balances safety, minimum energy, and dynamic feasibility, these parameters need to be adjusted appropriately. In path planning, safety is of highest priority. Therefore, we fix k_c to 1 to ensure that the planned trajectory is collision-free. We first set $k_f = 0$ and only adjust k_e with a step size of 0.5. The trajectory planning results are shown in Figs. R1-R2 and Table R1.

TABLE R1: The max distance between the quadrotor and the side surface of the obstacle under different k_e

k_e	0	0.5	1	1.5	2	2.5	3	3.5
Max Distance (m)	1.08	0.78	0.86	0.67	0.69	0.79	0.53	0.49

It can be observed that when $k_e = 0$, only the safety is considered. The trajectory is collision-free without considering smoothness. As k_e increased, the acceleration becomes smoother, and the trajectory continuity is improved. However, the weight of F_e in the function increases, while the weight of F_c decreases. If k_e becomes too large, it may negatively threaten the safety of the trajectory. When $k_e > 2.5$, the acceleration smoothness improves slightly, the maximum distance of the quadrotor to the obstacle surface (represents safety) is

E-mail: sy2203122@buaa.edu.cn, xiangyu_buaa@buaa.edu.cn.

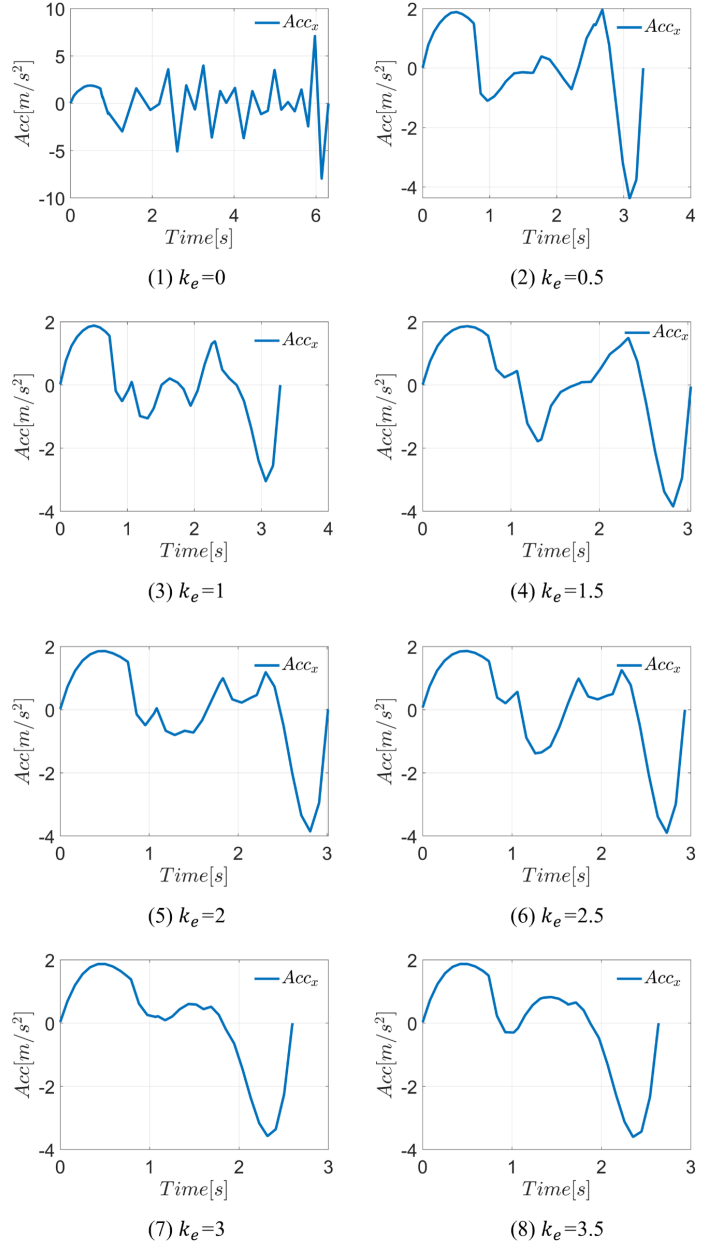


Fig. R1: (1)-(8) The planning acceleration of the quadrotor under different k_e

significantly decreased. Therefore, the optimal value for k_e is selected as 2.5, balancing acceleration smoothness and safety.

Following this, with $k_e = 2.5$ and $k_c = 1$ held constant, we adjust k_f by 0.5 at each step and the trajectory planning

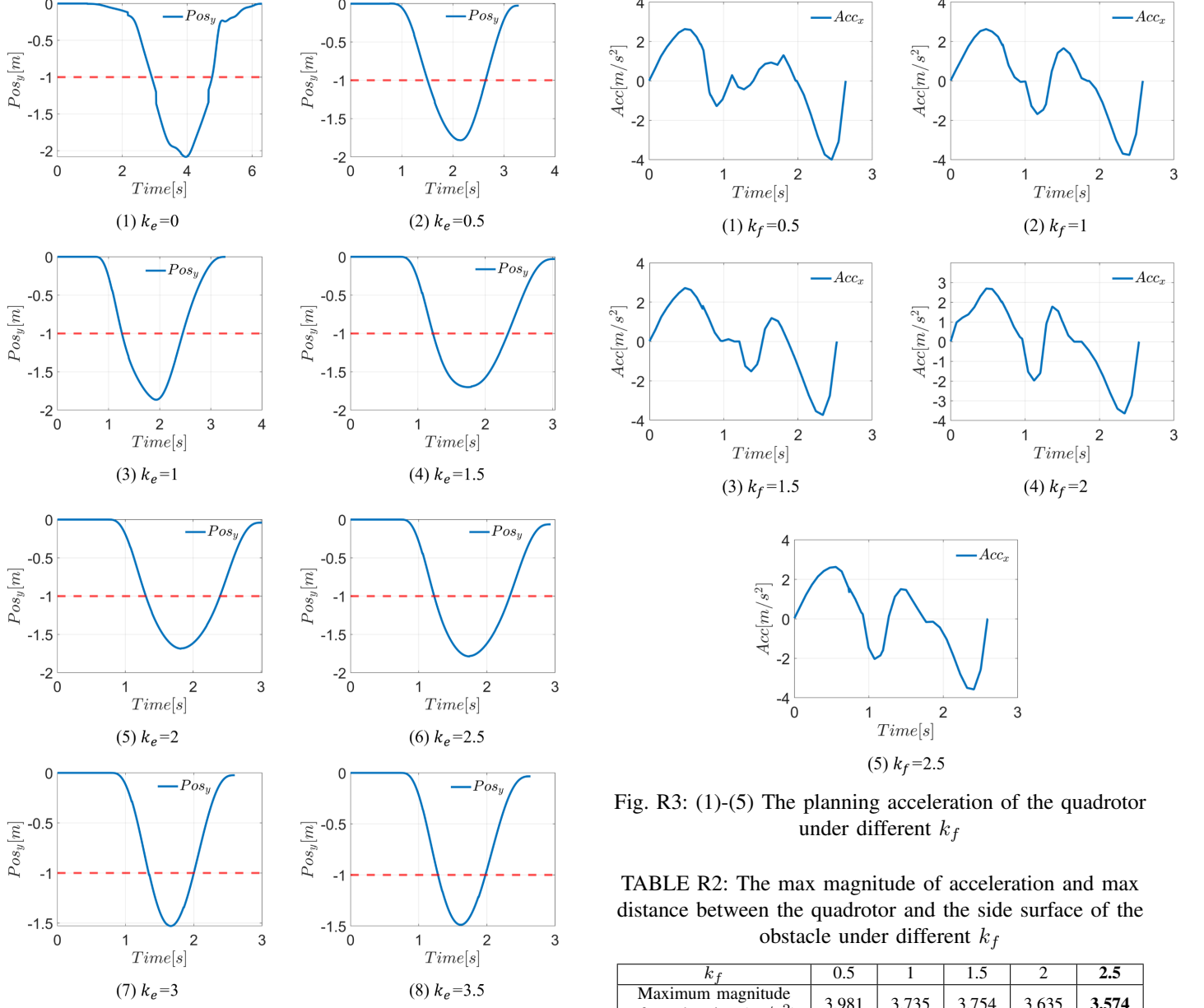


Fig. R2: (1)-(8) The position of the quadrotor in y direction under different k_e

results are depicted in Figs. R3-R4 and Table R2.

In the presence of the maximum acceleration magnitude constraint ($3m/s^2$), increasing k_f can reduce the magnitude of the maximum acceleration. When $k_f > 2$, the maximum distance of the quadrotor to the obstacle surface starts to significantly decrease, while the reduction effect on the maximum acceleration becomes limited. Therefore, the optimal value for k_f is selected as 2, ensuring that the acceleration remains reasonably constrained without significantly compromising safety.

The weights are finally determined as $k_f = 2, k_e = 2.5, k_c = 1$. Note that these parameters are part of the trajectory planning optimization and are independent of the quadrotor model.

Fig. R3: (1)-(5) The planning acceleration of the quadrotor under different k_f

TABLE R2: The max magnitude of acceleration and max distance between the quadrotor and the side surface of the obstacle under different k_f

k_f	0.5	1	1.5	2	2.5
Maximum magnitude of acceleration (m/s^2)	3.981	3.735	3.754	3.635	3.574
Max Distance from the surface (m)	0.774	0.752	0.639	0.586	0.502

C. The weights in the front-end W-A* algorithm

The proposed W-A* algorithm in Section IV.A includes three positive constants k_5, k_6, k_7 to be designed. They account for the computational time of the algorithm while assigning appropriate penalties to risk areas. The admissible range of values for these parameters are given as: $k_5 \subseteq (0, 25)$, $k_6 \subseteq (0, 0.4)$, $k_7 \subseteq (5, 30)$. In the following analysis, only the wind speed in the y direction is considered. Furthermore, we only analyze the case when v_w^y is positive. The analysis process remains the same when v_w^y is negative.

From Eqs. (14-16) in original paper, it can be observed that as the wind speed v_w^y increases, the risk area $[\mathcal{G}_o^y + \alpha_{y-}, \mathcal{G}_o^y + \alpha_{y+}]$ around the obstacle \mathcal{G}_o^y also expands. In both the simulation and experiments, the maximum lateral

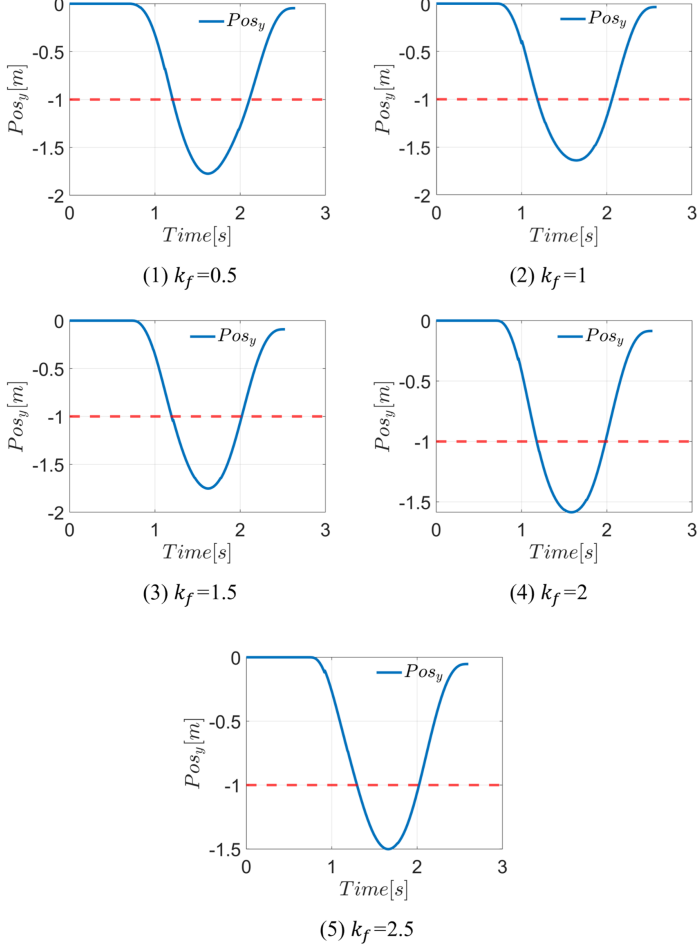


Fig. R4: (1)-(5) The position of the quadrotor in y direction under different k_f

wind speed v_w^y is set to $v_w^{max} = 8m/s$. In this case of v_w^{max} , the values of $\alpha_{y-}^{max} = -3$ and $\alpha_{y+}^{max} = 13$ can be obtained through Eqs. (14-16). Therefore, we can obtain the maximum risk area range around \mathcal{G}_o^y

$$\mathcal{G}_j^y \subseteq [\mathcal{G}_o^y - 3, \mathcal{G}_o^y + 13]. \quad (\text{R1})$$

For all $0m/s < v_w^y < v_w^{max}$, the risk area lies within this range. The definitions of k_5, k_6, k_7 are given by Eq. (17) in the original paper, which is equivalent to

$$G_1(\alpha_y) = k_5 e^{-k_6 |\alpha_y|} + k_7, \quad (\text{R2})$$

$$\alpha_y \subseteq [\alpha_{y-}^{max}, \alpha_{y+}^{max}] = [-3, 13].$$

k_6 determines the rate of decay of the risk value G_1 with increasing distance from the obstacle surface. When k_6 is small, the risk value decays slowly. As k_6 increases, the rate of decay accelerates. A smaller value of k_6 should be selected when we aim to achieve a more uniform risk value around the obstacle. For example, the risk values around the obstacle are all k_5+k_7 when $k_6 = 0$. We adjust the value of k_6 and observe the changes in the function $f(\alpha_y) = e^{-k_6 |\alpha_y|}$, $\alpha_y \subseteq [-3, 13]$. The result is shown in Fig. R5.

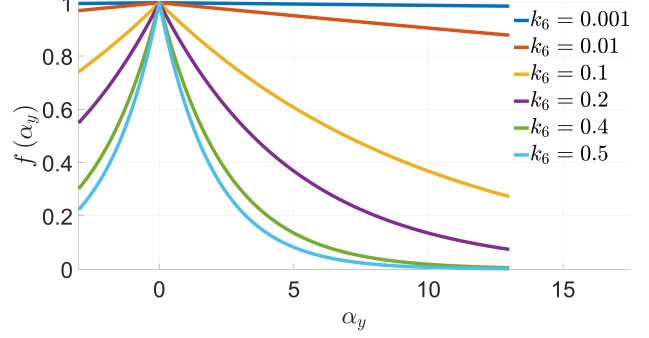


Fig. R5: The changes of $f(\alpha_y)$ when k_6 varies

TABLE R3: The planning results of the W-A* algorithm under different k_5

k_5	0	5	10	15	20	25	30
Pass through which side	Lee side	Windward					

It can be observed that when $k_6 = 0.4$, $f(\alpha_y)$ varies from 0 to 1 within $[\alpha_{y+}^{max}]$. If k_6 is larger, $f(\alpha_y)$ will decay to 0 before reaching the boundary α_{y+}^{max} . Therefore, the maximum value of k_6 is set to 0.4.

Further, we find the admissible range of k_5 and k_7 with $k_6 = 0.4$ held constant. From the form $G_1(\alpha_y) = f(\alpha_y) \cdot k_5 + k_7$, we can conclude that on the surface of the obstacle, the risk value is $G_1(0) = k_5 + k_7$. Besides, since $k_6 = 0.4$, $f(\alpha_{y+}^{max}) = 0$ and thus the risk value at α_{y+}^{max} is $G_1(\alpha_{y+}^{max}) = k_7$. To facilitate the adjustment of the two constants, we fix $k_5 + k_7 = 30$ and gradually adjust k_5 to observe the results of W-A*.

The simulation setup is described as follows: (1) The size of each grid cell is $0.1m \times 0.1m$. A rectangle obstacle with dimensions $2m \times 3m$ is placed in the environment, with center positions of [5,5] m. (2) The wind speed is set as $\hat{v}_w^y = v_w^y = 8m/s$, which blows from leftward.

The starting point and the endpoint of the quadrotor are set as [2, 4]m and [8, 5]m. Note that the given starting point is slightly offset from the center of the obstacle in the y direction. This is designed to verify that even if the initial position of the quadrotor is close to the windward side, it can still pass through the lee side of the obstacle under windy conditions. The planning results of the W-A* algorithm under different k_5 is shown in Table R3.

Therefore, the admissible range of k_5 is (0, 25). Since $k_5 + k_7 = 30$, the range of k_7 is (5, 30).

When $k_5 = 5, k_6 = 0.001, k_7 = 25$ provided in the paper are applied, all the risk values around the obstacle remain close to 30. It is designed to ensure the quadrotor can pass through from the lee side during the experiment.

D. The observer gains

First, we need to determine the appropriate gain matrix L for the WSO. When the gain matrix L for WSO is set to a larger value, the convergence performance improves. However, in practical experiments, the quadrotors are subjected to various

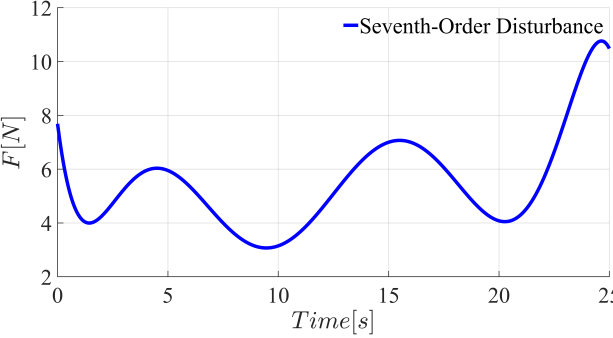


Fig. R6: The 7th-order disturbance need to have six extremum points within the time range

sources of noise. When the gain is set too high, the noise will be amplified. It potentially leads to system divergence [3]. Therefore, the value of L should not be too large. In the experiment, we suggest gradually reducing the value of $\lambda_{max}(L)$ from a small starting point until the critical value is reached, where the quadrotor begins to vibrate at high frequencies [4]. In our quadrotor platform, the chosen value of $L = diag(0.5, 0.5, 0.5)$ is found to offer excellent observational results while avoiding significant noise amplification.

Once the matrix L for the WSO is selected, it results in a root. In the proposed IWSO observer, the number of roots is increased due to the use of integration. Therefore, the matrices L_2 , L_1 , and L_0 must be selected to ensure that the roots of their characteristic equation are the same as the root of L . This is designed to fairly compare the impact of the number of roots on the estimation performance. Thus, the diagonal gain matrices corresponding to the proposed IWSO in our platform are set as $L_2 = diag(1.5, 1.5, 1.5)$, $L_1 = diag(0.75, 0.75, 0.75)$, $L_0 = diag(0.125, 0.125, 0.125)$.

If the platform is changed, the method for tuning these parameters remains the same, though their values may differ.

E. Time sliding window t_w

The selection of t_w depends on the desired state of the quadrotor, the external wind disturbance, and the choice of observer gain matrices according to Eq. (9) in the original paper. When t_w is small, the overshoot decreases. When $t_w = 0s$, the integral term becomes zero. The IWSO degenerates to the WSO, resulting in a larger time delay (it is defined in Section VI.C). As t_w increases, the value of the integral term increases as well. The IWSO increases certain values through integration, which are used to compensate for the time delay effect. When the integral term is larger, t_w should be smaller, and vice versa. According to Eq. (9), the integral term includes the actual state (which is affected by external wind disturbances), the desired state, and the parameter matrices L_2 , L_1 , and L_0 . All of them specifically affect the choice of t_w .

Intuitively, if the desired speed of the quadrotor is large or external disturbances vary significantly, t_w should be relatively larger. When the observer's gain matrices increase, t_w should be reduced. In the experiments and simulations, we adjust t_w

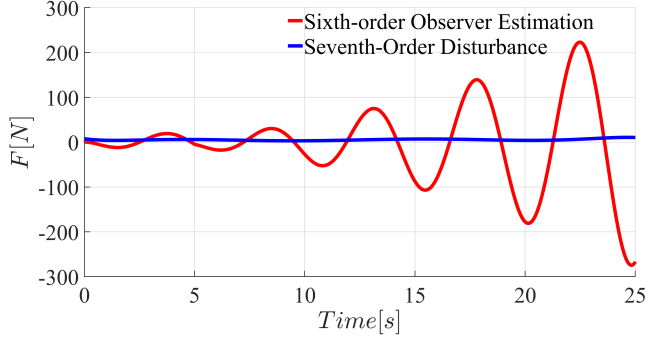


Fig. R7: The effect of using a 6th-order observer to estimate a 7th-order disturbance

from a small starting point in discrete steps to choose the optimal t_w according to the guidelines above.

II. THE REASON FOR EMPLOYING A SEVENTH-ORDER IWSO IN SIMULATION

In the simulation, the time range is set from 0 to 25 seconds. Aiming to demonstrate the effects of different order disturbances, all extremum points of the disturbance must be displayed within the 25-second interval. For example, a 7th-order disturbance requires 6 extremum points within the time range (Fig. R6).

As the order of the disturbance increases, the complexity of the function also increases. When the disturbance is set to 7th-order, the function becomes very complex

$$\begin{aligned} F(t) = & -1.94712845535921 \cdot 10^{-6} \cdot t^7 + 1.72198869604469 \cdot 10^{-4} \cdot t^6 \\ & - 5.96490697906819 \cdot 10^{-3} \cdot t^5 + 0.102200130575888 \cdot t^4 \\ & - 0.898587003628853 \cdot t^3 + 3.80371750780161 \cdot t^2 \\ & - 6.45591931724366 \cdot t + 7.68551879496219. \end{aligned} \quad (R3)$$

Considering the design requirements, we set the upper limit of the disturbance order to 7. It allows us to demonstrate the validity of the proposed method while reducing design complexity. Additionally, when the order of the observer is set to n , the observer can effectively estimate disturbances with order less than or equal to n . However, disturbances with order greater than n will lead to divergence in the estimation. For example, the effect of using a 6th-order observer to estimate a 7th-order disturbance is shown in Fig. R7.

Therefore, when the upper limit of the disturbance order is set to 7, we also set the corresponding observer order to 7. While higher-order observers can be employed, they would increase system complexity and result in excessive computational resource consumption.

III. THE SUPPLEMENTARY PROOF OF THEOREM 1

In *Theorem 1*, it is proven that \tilde{v}_w exhibits exponential convergence in the case of distinct and negative roots.

In the experiments, the matrix L is chosen such that the root of the WSO is -0.5 and L_2 , L_1 , L_0 are selected to ensure that all three roots of the IWSO are all -0.5. Keep the magnitude of the characteristic roots unchanged, allowing for a variation

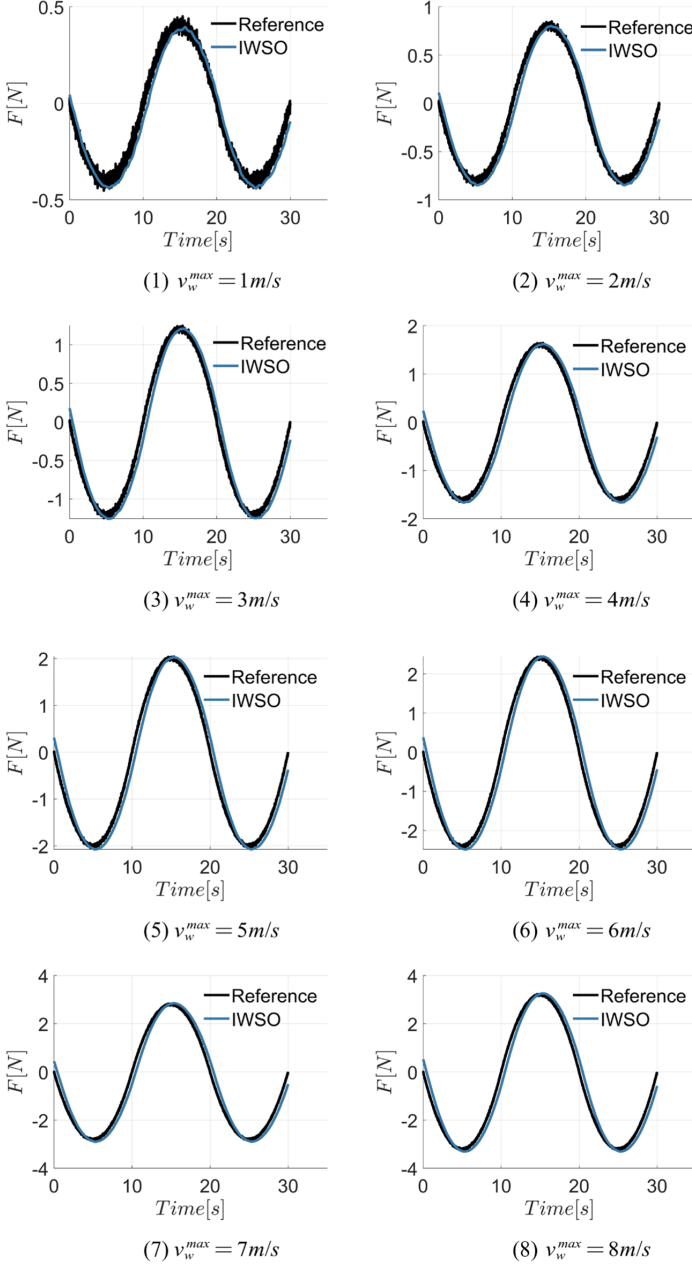


Fig. R8: (1)-(8) The performance of IWSO observer in estimating the disturbance force in the x direction under different v_w^{\max} (m/s)

TABLE R4: The estimation performance (Root mean square error (RMSE)) of IWSO under different v_w^{\max} (m/s)

v_w^{\max} (m/s)	1	2	3	4	5	6	7	8
RMSE (N)	0.05	0.09	0.13	0.17	0.21	0.25	0.29	0.33

in the number of roots. This is done in order to fairly compare the real-time performance of the IWSO relative to the WSO.

This deviates from the case of distinct characteristic roots as presented in *Theorem 1*. Here, we have added a proof showing that even in the presence of repeated roots, \tilde{v}_w still satisfies exponential convergence.

Suppose that after solving the characteristic equation, each of the x , y , and z directions has $m_x, m_y, m_z \in (2, 3)$ multiple negative roots. The solution of the differential equation is:

$$\tilde{v}_w = \begin{bmatrix} \sum_{i=1}^{m_x} c_{1i} t^{i-1} e^{-\mu_{1i} t} + \sum_{j=m_x+1}^3 c_{1j} e^{-\mu_{1j} t} \\ \sum_{i=1}^{m_y} c_{2i} t^{i-1} e^{-\mu_{2i} t} + \sum_{j=m_y+1}^3 c_{2j} e^{-\mu_{2j} t} \\ \sum_{i=1}^{m_z} c_{3i} t^{i-1} e^{-\mu_{3i} t} + \sum_{j=m_z+1}^3 c_{3j} e^{-\mu_{3j} t} \end{bmatrix}^T, \quad (R4)$$

where $\mu_{ij} > 0$.

To prove that $\|\tilde{v}_w\|^2 = \|\tilde{v}_w^x\|^2 + \|\tilde{v}_w^y\|^2 + \|\tilde{v}_w^z\|^2$ exhibits exponential convergence, we first consider one direction, use the x direction as an example

$$\begin{aligned} \tilde{v}_w^x &= (c_{11} + c_{12}t + c_{13}t^2) e^{-\mu_{11}t}, \\ &\text{or} \\ \tilde{v}_w^x &= (c_{11} + c_{12}t) e^{-\mu_{11}t} + c_{13}e^{-\mu_{12}t}. \end{aligned} \quad (R5)$$

The solution exists in two forms.

$$(1) \tilde{v}_w^x = (c_{11} + c_{12}t + c_{13}t^2) e^{-\mu_{11}t} :$$

$$\begin{aligned} \|\tilde{v}_w^x\|^2 &= (c_{11} + c_{12}t + c_{13}t^2)^2 e^{-2\mu_{11}t} \\ &= (c_{11} + c_{12}t + c_{13}t^2)^2 e^{-\mu_{11}t} \cdot e^{-\mu_{11}t} \\ &= f(t) \cdot e^{-\mu_{11}t}, \\ \dot{f}(t) &= [-\mu_{11}c_{13}^2 t^4 + k_3 t^3 + k_2 t^2 + k_1 t + k_0] \cdot e^{-\mu_{11}t} \\ &= h(t) e^{-\mu_{11}t}. \end{aligned} \quad (R6)$$

It can be observed that $h(t)$ is a polynomial with the highest-degree term having a negative coefficient. Therefore, as $t \rightarrow \infty$, both $h(t)$ and its derivatives tend to negative infinity.

$$\begin{aligned} h(t) &= -\mu_{11}c_{13}^2 t^4 + k_3 t^3 + k_2 t^2 + k_1 t + k_0 \\ \dot{h}(t) &= -4\mu_{11}c_{13}^2 t^3 + 3k_3 t^2 + 2k_2 t + k_1 \\ \ddot{h}(t) &= -12\mu_{11}c_{13}^2 t^2 + 6k_3 t + 2k_2 \\ h(t)^{(3)} &= -24\mu_{11}c_{13}^2 t + 6k_3 \\ h(t)^{(4)} &= -24\mu_{11}c_{13}^2 \end{aligned} \quad (R7)$$

$h(t)^{(4)}$ is always negative for $t > 0$, which implies that $h(t)^{(3)}$ is decreasing. Therefore, there exists a moment t_4 such that for $t > t_4$, $h(t)^{(3)}$ is negative. This leads to the conclusion that $\dot{h}(t)$ begins to decrease when $t > t_4$. And there exists a moment t_3 such that for $t > t_3 > t_4$, $\dot{h}(t)$ is negative. By similar reasoning, we find that there exists a moment t_1 such that for $t > t_1 > t_2 > t_3 > t_4$, $h(t)$ remains negative.

Since $e^{-\mu_{11}t} > 0$ for $t > 0$, it follows that when $t > t_1$, $\dot{f}(t) = h(t) e^{-\mu_{11}t}$ is negative. It means that $f(t)$ is decreasing. In addition, it should be noted that $t \rightarrow \infty, f(t) \rightarrow 0^+$. Therefore, there exists a moment $t_0 \geq t_1$ such that for $t > t_0 \geq t_1$, $f(t) < 1$.

It can be concluded that for $t > t_0 \geq t_1$

$$\|\tilde{v}_w^x\|^2 = f(t) \cdot e^{-\mu_{11}t} < e^{-\mu_{11}t}. \quad (R8)$$

$$(2) \tilde{v}_w^x = (c_{11} + c_{12}t) e^{-\mu_{11}t} + c_{13}e^{-\mu_{12}t}:$$

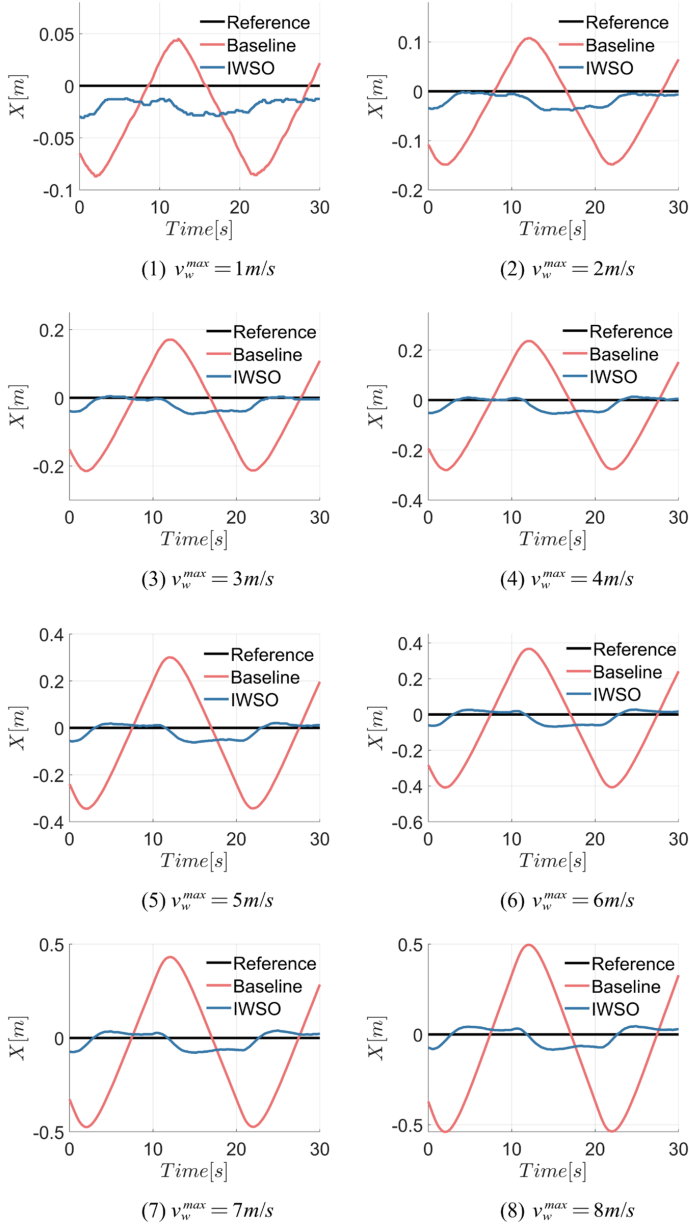


Fig. R9: (1)-(8) The tracking performance in the x direction of the quadrotor under different v_w^{max}

$$\begin{aligned} \|\tilde{v}_w^x\|^2 &= [(c_{11} + c_{12}t)e^{-\mu_{11}t} + c_{13}e^{-\mu_{12}t}]^2 \\ &\leq [(c_{11} + c_{12}t)^2 + 2c_{13}(c_{11} + c_{12}t) + c_{13}^2]e^{-2\mu_{11}t} \\ &= (c_{12}^2t^2 + l_1t + l_0)e^{-2\mu_{11}t} \\ &= (c_{12}^2t^2 + l_1t + l_0)e^{-\mu_{11}min t} \cdot e^{-\mu_{11}min t}, \\ &= f(t) \cdot e^{-\mu_{11}min t} \\ \dot{f}(t) &= [-\mu_{11}c_{12}^2t^2 + k_1t + k_0] \cdot e^{-\mu_{11}min t} \\ &= h(t) e^{-\mu_{11}min t}, \end{aligned} \quad (R9)$$

where $\mu_{11}min = \min(\mu_{11}, \mu_{12})$.

It can be observed that $h(t)$ is a polynomial with the highest-degree term having a negative coefficient. Therefore, as $t \rightarrow$

∞ , both $h(t)$ and its derivatives tend to negative infinity.

$$\begin{aligned} h(t) &= -\mu_{11}c_{12}^2t^2 + k_1t + k_0 \\ \dot{h}(t) &= -2\mu_{11}c_{12}^2t + k_1 \\ \ddot{h}(t) &= -6\mu_{11}c_{12}^2 \end{aligned} \quad (R10)$$

$\ddot{h}(t)$ is always negative for $t > 0$, which implies that $\dot{h}(t)$ is decreasing. Therefore, there exists a moment t_2 such that for $t > t_2$, $\dot{h}(t)$ is negative. This leads to the conclusion that $h(t)$ begins to decrease when $t > t_2$. And there exists a moment t_1 such that for $t > t_1 > t_2$, $h(t)$ is negative.

Since $e^{-\mu_{11}min t} > 0$ for $t > 0$, it follows that when $t > t_1$, $\dot{f}(t) = h(t)e^{-\mu_{11}min t}$ is negative. It means that $f(t)$ is decreasing. In addition, it should be noted that $t \rightarrow \infty$, $f(t) \rightarrow 0^+$. Therefore, there exists a moment $t_0 \geq t_1$ such that for $t > t_0 \geq t_1$, $f(t) < 1$.

It can be concluded that for $t > t_0 \geq t_1$

$$\|\tilde{v}_w^x\|^2 = f(t) \cdot e^{-\mu_{11}min t} < e^{-\mu_{11}min t}. \quad (R11)$$

Therefore, it can be concluded that when there are multiple roots, each component in every direction satisfies exponential convergence.

In the absence of multiple roots, a similar approach can be used to prove the convergence of the components when $\tilde{v}_w^x = c_{11}e^{-\mu_{11}t} + c_{12}e^{-\mu_{12}t} + c_{13}e^{-\mu_{13}t}$,

$$\begin{aligned} \|\tilde{v}_w^x\|^2 &= [c_{11}e^{-\mu_{11}t} + c_{12}e^{-\mu_{12}t} + c_{13}e^{-\mu_{13}t}]^2 \\ &\leq \left(\sum_{j=1}^3 c_{1j}^2 + 2c_{11}c_{12} + 2c_{11}c_{13} + 2c_{12}c_{13} \right) e^{-2\mu_{11}min t}, \\ &= f(t) \cdot e^{-\mu_{11}min t} \end{aligned} \quad (R12)$$

where $\mu_{11}min = \min(\mu_{11}, \mu_{12}, \mu_{13})$. It is obvious that there exists a moment $t_0 > 0$ such that for $t > t_0$, $\|\tilde{v}_w^x\|^2 \leq e^{-\mu_{11}min t}$.

Taking into account the x , y , and z directions, for each direction, there exists a moment such that the following condition holds:

$$\begin{cases} \|\tilde{v}_w^x\|^2 < e^{-\mu_{11}min t} & t > t_0^x \\ \|\tilde{v}_w^y\|^2 < e^{-\mu_{22}min t} & t > t_0^y \\ \|\tilde{v}_w^z\|^2 < e^{-\mu_{33}min t} & t > t_0^z \end{cases} . \quad (R13)$$

Thus, when $t > \max(t_0^x, t_0^y, t_0^z)$, $\|\tilde{v}_w\|^2 \leq e^{-\mu_{11}min t} + e^{-\mu_{22}min t} + e^{-\mu_{33}min t} \leq 3e^{-\min(\mu_{11}min, \mu_{22}min, \mu_{33}min)t}$.

Obviously, the estimated error \tilde{v}_w will converge to zero exponentially.

When using L_2 , L_1 , and L_0 as taken from the paper, the characteristic equation is given by

$$\begin{aligned} \mu^3 + L_2\mu^2 + L_1\mu + L_0 &= \begin{bmatrix} (\mu_1 + 0.5)^3 & & \\ & (\mu_2 + 0.5)^3 & \\ & & (\mu_3 + 0.5)^3 \end{bmatrix}. \end{aligned} \quad (R14)$$

The roots are all repeated and negative, satisfying the conditions.

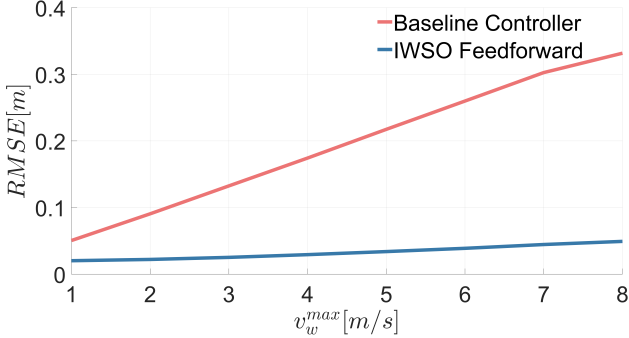


Fig. R10: The position tracking accuracy (RMSE) under different v_w^{max}

IV. THE SIMULATION IN DIFFERENT WIND SPEEDS

A. IWSO observer

Under different wind speed ($1\text{m}/\text{s} - 8\text{m}/\text{s}$), the estimation performance of IWSO is excellent. Furthermore, the IWSO feedforward controller can significantly improve the position tracking accuracy of the quadrotor.

The external wind speed $\mathbf{v}_w = [v_w^x, v_w^y, 0]$ varies in a quadratic form, expressed as follows

$$\begin{aligned} v_w^x(t) &= 0.05 \cdot \text{randn}(\cdot) + v_w^{max} \cdot \begin{cases} \frac{1}{25}t(t-10), & 0 < t \leq 10 \\ -\frac{1}{25}(t-10)(t-20), & 10 < t \leq 20 \\ \frac{1}{25}(t-20)(t-30), & 20 < t \leq 30, \end{cases} \\ v_w^y(t) &= 0.05 \cdot \text{randn}(\cdot) + v_w^{max} \cdot \begin{cases} -\frac{1}{25}t(t-10), & 0 < t \leq 10 \\ \frac{1}{25}(t-10)(t-20), & 10 < t \leq 20 \\ -\frac{1}{25}(t-20)(t-30), & 20 < t \leq 30, \end{cases} \end{aligned} \quad (\text{R15})$$

where v_w^{max} starts at $1\text{m}/\text{s}$ and increases by $1\text{m}/\text{s}$ intervals up to $8\text{m}/\text{s}$ and $0.05 \cdot \text{randn}(\cdot)$ represents random noise with a mean of 0 and a standard deviation of 0.05, drawn from a normal distribution. It can be seen from Eq. (8) in the original paper that the disturbance induced by the external wind speed \mathbf{v}_w is

$$\mathbf{F}_w = \mathbf{RAR}^T \mathbf{v}_w. \quad (\text{R16})$$

The desired state of the quadrotor is set to hover. The performance of IWSO observer in estimating the disturbance force in the x direction under different v_w^{max} is shown in Fig. R8 and Table R4.

Furthermore, we use both the baseline controller and the IWSO feedforward controller to maintain the desired state. The position tracking indices in the x direction under different v_w^{max} is shown in Fig. R9.

The position tracking accuracy is defined as follows

$$RMSE = \sqrt{\frac{1}{M} \sum_{i=1}^M \|\mathbf{p}_i - \mathbf{p}_{di}\|^2}, \quad (\text{R17})$$

where M is the size of the dataset collected during the simulation, \mathbf{p}_i and \mathbf{p}_{di} represent the real and desired position of the quadrotor, respectively.

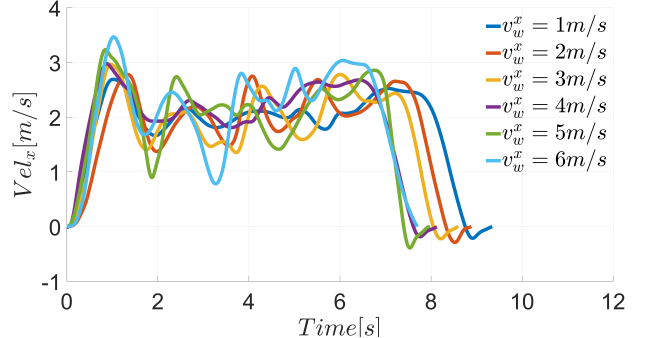


Fig. R11: The velocity of the quadrotor during flight under different v_w^x

TABLE R5: The maximum velocity, acceleration, and energy throughout the entire flight under different v_w^{max}

v_w^{max} (m/s)	1	2	3	4	5	6
Max Vel (m/s)	2.69	2.78	2.96	2.98	3.23	3.46
Max Acc (m/s ²)	4.07	4.33	4.82	5.31	5.85	6.11
Energy (J)	256.47	251.80	251.37	238.95	235.56	229.21

We calculate the position tracking accuracy when using the baseline controller and the IWSO feedforward controller. The results are shown in Fig. R10. It can be observed that when v_w^{max} changes, the IWSO feedforward controller can significantly improve the position tracking accuracy of the quadrotor. This validates the effectiveness of the proposed method under different wind speeds.

B. Planner

First, the varying forward wind v_w^x is involved to investigate its impact on the proposed wind utilization concept. The environment featured a forward wind v_w^x , where v_w^x starts at $1\text{m}/\text{s}$ and increases by $1\text{m}/\text{s}$ intervals up to $6\text{m}/\text{s}$. The maximum velocity, acceleration, and energy throughout the entire flight are calculated. The results are shown in Fig. R11 and Table R5.

As v_w^x increases, the maximum velocity and acceleration during the whole flight are increased, while the energy consumption is decreased. The effectiveness of the wind utilization concept becomes increasingly efficient with higher v_w^x .

Next, the lateral wind speed v_w^y is adjusted to investigate its impact on the proposed W-A* algorithm. The environment featured a lateral wind v_w^y , where v_w^y starts at $1\text{m}/\text{s}$ and increases by $1\text{m}/\text{s}$ intervals up to $6\text{m}/\text{s}$. The map contains two columns with ten rectangular prism obstacles. There are leftward winds in the region where $y > 0$, and the wind direction is reversed in the region where $y < 0$. We analyze the successful rate of the quadrotor planning on the lee side of obstacles as v_w^y changes. The results are shown in Fig. R12 and Table R6.

When v_w^y is low, the W-A* algorithm does not exhibit a tendency to plan paths toward the lee side. As described by Eqs.

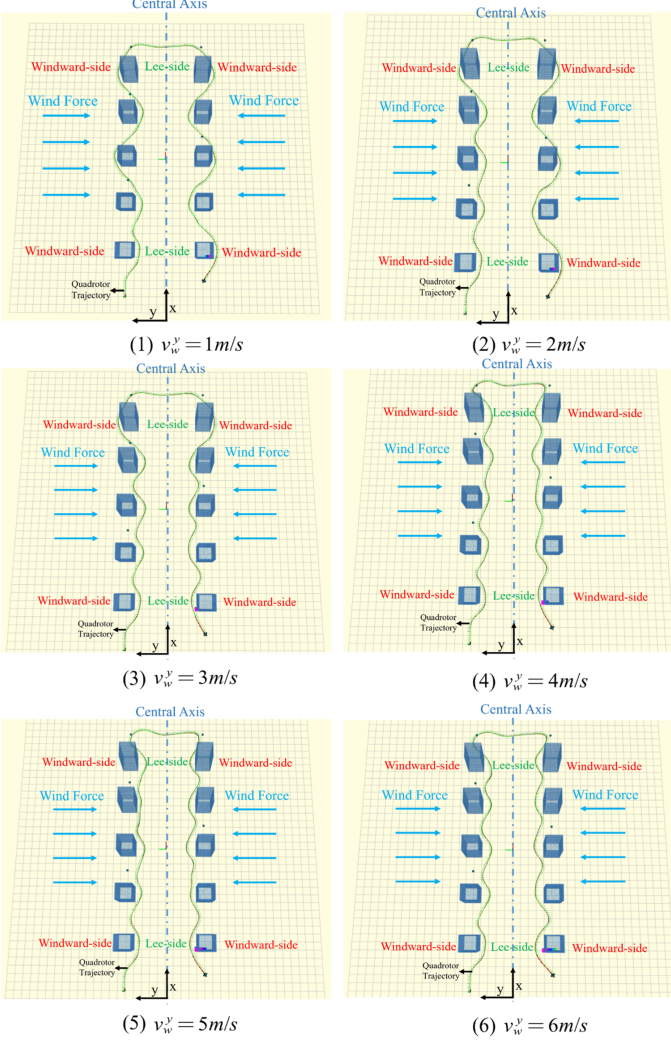


Fig. R12: (1)-(6) The flight trajectory of the quadrotor under different v_w^y when using the W-A* algorithm

TABLE R6: The successful rate of the quadrotor planning at the lee side of obstacles under different v_w^y

v_w^y (m/s)	1	2	3	4	5	6
Lee side rate	50%	60%	80%	100%	100%	100%

(14-17) in the original paper, the risk term in the windward region of obstacles is small under low wind speed conditions. As v_w^y increases, the risk term on the windward side gradually grows, and the advantages of the W-A* algorithm become more apparent. When v_w^y reaches 4 m/s, the rate of planning toward the lee side reaches 100%. As v_w^y continues to rise, the quadrotor can consistently plan its path toward the lee side.

REFERENCES

- [1] H. Jeon, J. Song, H. Lee, and Y. Eun, "Modeling quadrotor dynamics in a wind field," *IEEE/ASME Transactions on Mechatronics*, vol. 26, no. 3, pp. 1401–1411, 2021.
- [2] J. Svacha, K. Mohanta, and V. Kumar, "Improving quadrotor trajectory tracking by compensating for aerodynamic effects," *2017 International Conference on Unmanned Aircraft Systems (ICUAS)*, pp. 860–866, 2017.

- [3] J. Jia, K. Guo, X. Yu, L. Guo, and L. Xie, "Agile flight control under multiple disturbances for quadrotor: Algorithms and evaluation," *IEEE Transactions on Aerospace and Electronic Systems*, vol. 58, no. 4, pp. 3049–3062, 2022.
- [4] J. Jia, W. Zhang, K. Guo, J. Wang, X. Yu, Y. Shi, and L. Guo, "EVOLVER: Online learning and prediction of disturbances for robot control," *IEEE Transactions on Robotics*, vol. 40, pp. 382–402, 2024.